

Modelling of a 50 MW_{th} On-Sun Reactor for SCWG of Algae: Understanding the Design Constraints

Mahesh B. Venkataraman^{1,a)}, Charles-Alexis Asselineau^{1,b)}, Alireza Rahbari^{1,c)} and John Pye^{1,d)}

¹*Research School of Engineering, The Australian National University, ACT 2601, Australia*

^{a)}mahesh.venkataraman@anu.edu.au

^{b)}charles-alexis.asselineau@anu.edu.au

^{c)}alireza.rahbari@anu.edu.au

^{d)}john.pye@anu.edu.au

Abstract. Thermochemical conversion of algae, using solar-assisted supercritical water gasification (SCWG), into liquid fuels is a promising route for reducing the greenhouse gas (GHG) emissions associated with the transportation sector. This study attempts to combine CST and SCWG, and identify the key constraints in designing a solar cavity receiver/reactor for on-sun SCWG of algae.

A detailed model of a tubular plug-flow receiver/reactor, operating at 24 MPa and 400–600°C with a solar input of 50 MW_{th} is presented here. An optimised polar heliostat field is designed using SolarPILOT, for developing a pseudo-steady state model for summer solstice noon conditions in Geraldton, WA, Australia. Monte-Carlo Ray Tracing is used to determine the flux distribution on the reactor tubes and also to determine the view-factor matrix. The radiosity calculations are coupled with the hydrodynamic model, which consists of equilibrium prediction, mixture property calculation, and heat/mass transfer in the reactor. A parametric evaluation of the steady state performance and quantification of the losses through wall conduction, external radiation and convection, internal convection, frictional pressure drop, mixing and chemical irreversibility, is presented. The model additionally incorporates material constraints based on the allowable stresses for a commercially available Ni-based alloys for the cavity reactor.

INTRODUCTION

Greenhouse gas (GHG) emissions from consumption of fossil-based liquid fuels currently accounts for almost one-third of the global anthropogenic GHG-emissions [1]. Hydrocarbon liquid fuels form a key part of the day-to-day operations for both the end users and the industries. Our reluctance in moving to a new zero-carbon fuel is understandable, and hence, the adoption of carbon-neutral synthetic fuels may be necessary, at least in the short-term, to reduce the anthropogenic CO₂-footprint. Carbon-neutral biofuels present an attractive opportunity in this regard, especially for long-range aviation and shipping.

Thermochemical conversion of biomass can provide carbon-neutral high calorific-value fuels (hydrogen, methane and/or syngas) for manufacturing, fuel cells, or subsequent conversion to liquid fuels via commercially available technologies such as Fischer–Tropsch, methanol or dimethyl ether synthesis. Several technologies for biofuel production, such as hydrothermal liquefaction, gasification, anaerobic digestion, and trans-esterification have received significant research interest. Supercritical water gasification (SCWG) can be argued as one of the most prospective option due to its flexibility of feedstock, low char formation, ability to utilise the entire biomass rather than just the lipid fraction, and the potential ease of scaling-up [2]. The nature of SCWG allows for feedstock with high moisture content, including, wood and forest residue, agricultural waste, municipal wastes and sewage sludge. However, a fuel production route capable of completely replacing fossil-based liquid fuels cannot be based on waste biomass streams only, primarily because of the de-centralised production and limited supply of biomass waste. Algae, as a farmed-biomass feedstock, can provide an attractive alternative. Compared to other biomass, algae has a higher growth rate, can be cultivated on non-arable land and in seawater, does not compete with food or infrastructure land (an issue which was highlighted in the 2008 Gallagher report [3] as a shortcoming of cultivated biomass). In addition to the experimental

proofs-of-concept, as discussed in a recent review [2], several researchers have also focused on system level modelling of the SCWG process for producing different end products, including synthetic natural gas [4], combined fuel and power [5], and liquid fuels [6].

Concentrated solar thermal (CST) provides an efficient way of converting the solar radiation into heat and has a huge potential for driving endothermic processes such as SCWG. The ability to grow biomass in high-irradiance regions close to the ocean, without any need for freshwater, is a great motivation for coupling CST with SCWG of algae. The limitations of conventional gasification in handling wet biomass makes the solar-SCWG process all the more attractive. However, the modelling and large scale implementations of solar-SCWG reactors are both at a nascent stage. Two SCWG systems driven by concentrating solar energy have been demonstrated at Xi'an Jiaotong University, China with a maximal throughput capacity of 16 kg/h. One of these systems uses a multi-dish irradiated tubular cavity reactor for H_2 -production via SCWG of biomass [7, 8]. The reactor is composed of preheating and reaction zones, to implement high heating rates of feedstock, and consequently, higher gasification efficiency. The second system has a toroidal heliostat coupled with a fluidised bed reactor for SCWG [7, 9, 10]. A pilot scale facility has also been established in the Ningxia Hui Autonomous Region, with the following design parameters: feedstock rate of 1.03 t/h and the design temperature and pressure of 800°C and 40 MPa respectively. The peak concentrated solar power was limited to 163 kW. Preliminary results showed a hydrogen production molar fraction >55% and thermal efficiency of 73.1% [10]. The solar reactor designs alleviate some challenges concerning the technical feasibility of SCWG process using concentrated solar energy but detailed modelling and optimisation of such experimental designs is desirable.

In a previous work [11], we presented a 1-d reactor model for carrying out on-sun SCWG, with a focus on assessing the feasibility. The work was limited by the assumption of constant flux distribution on the reactor walls and did not account for thermal stresses. Even with these simplistic assumptions, the identified feasibility region, given the poor heat-transfer in supercritical medium and thermal stresses, was quite small. In this work, we include the design of the heliostat field, with an optimum aiming strategy, and calculate a realistic flux distribution on the reactor tubes. Monte-Carlo ray tracing is used for calculating the view-factors and a radiosity model is incorporated. Further improvements to the hydrodynamic model are presented with the inclusion of mixture transport properties. Based on this model, a parametric evaluation of the gasification and thermal energy efficiency of solar-SCWG reactor is presented.

MODEL DESCRIPTION

The system considered here is composed of a heliostat field and a cavity reactor positioned on top of a tower at 100 m above the pivot point height of the heliostats. A schematic showing the tower and receiver orientation with respect to the heliostat field is shown in Fig. 1(a). The location is assumed to be Geraldton (WA, Australia) and the size of the heliostat field is sufficient for providing a thermal power input of 50 MW_{th} to a hemi-cylindrical cavity (17.0 m outer diameter x 26.7 m height) receiver. As reported in our previous study [11], the operating conditions of the reactor impose strict constraints on the maximum peak flux acceptable on the tubes. The cavity reactor concept is chosen in an attempt to establish a design point flux distribution able to meet this strict requirement (here assumed at 130 kW/m²) without dramatically increasing the reactor area exposed to the surroundings which would result in vastly increased thermal emission losses. For such a cavity receiver, a polar arrangement is deemed suitable for a 50 MW_{th} capacity.

The heliostat field layout is established using NREL's tool, SolarPILOT (version 1.1) [12]. The system is then ray-traced using the SolTRACE engine in SolarPILOT for summer solstice noon conditions. The ray-data from SolTRACE incident on the aperture plane of the cavity were saved, and then re-sampled to run with Tracer [13, 14] in order to evaluate a range of hemi-cylindrical cavity dimensions. The specific dimensions of the reactor in this study were then determined using an iterative process involving establishing an adequate aiming strategy using SolarPILOT and then iterating on the dimensions of the reactor: the diameter, the height and the aperture width and height. The specific aiming strategy used in this study is the "image size priority" heuristic included in SolarPILOT and the selected strategy with aiming parameter values of (15, 4) in the x,y directions. The aiming parameter accounts for the minimum standard deviation multiplier offset to each heliostat focal image from the reactor edge and determines an authorised aiming region for each heliostat depending on the size of their image (more detailed explanation is available in the SolarPILOT manual). The resulting reactor location and geometry are presented in Fig. 1(b). The chosen aiming strategy results in a large vertical high flux area as shown in Fig. 2(a), useful in offering aiming space for the heliostats without increasing the diameter of the hemi-cylinder. The aperture shape and dimensions are then chosen accordingly,

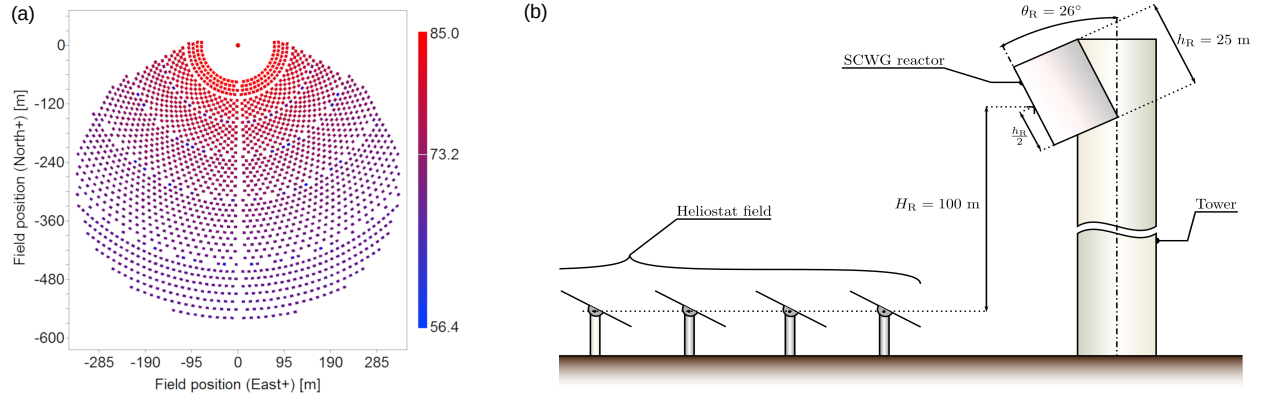


FIGURE 1. (a) Layout of the optimised heliostat field. The color map reflects the optical efficiency of individual heliostats (b) System diagram showing the heliostat, tower and receiver.

resulting in more homogeneous flux distributions compared to a horizontal aiming arrangement. A schematic showing the cross section of the cavity (as viewed from the top) is shown in Fig. 2(b). The curved wall of the cavity is covered with 8 tube banks each containing 125 parallel vertical reactor tubes.

The radiative heat transfer processes are approximated using a semigray assumption with two spectral regions [15]. The shorter wavelengths region corresponding to the solar radiation spectrum is evaluated independently from the thermal emissions of the hot surfaces of the receiver, occurring at longer wavelengths. A range of optical simulation methods are used in this study to obtain the short wavelength component of the radiation in the system, assumed independent of the temperature. Both the determination of the heliostat field layout and the reactor dimensions require the estimation of concentrated solar radiation distributions at the reactor location.

The flux distribution obtained from the optical simulations serves as a source term in the energy balance of the reactor, based on Venkataraman et al. [11] and modified to take into account the geometrical effects of the radiative heat transfer contribution as in Asselineau et al. [16]. The net radiation method [15] is used to evaluate the longer wavelengths contribution and the required view-factors matrix established using MCRT. The optical design parameters used in the study are summarised in Table 1.

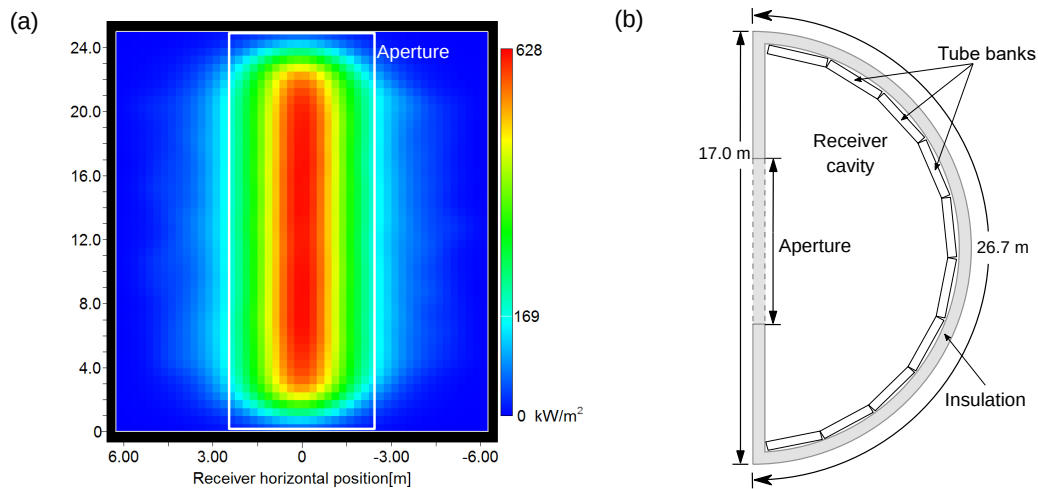


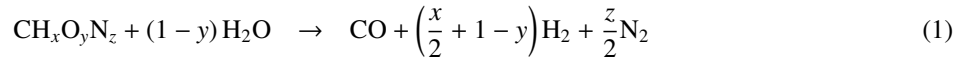
FIGURE 2. (a) Incident flux on the aperture plane, (b) Schematic showing the cross-section of the receiver/reactor (as viewed from top),

The concentrated solar radiation is used to increase the temperature of heat transfer fluid — 15.16 wt.% algae solution

TABLE 1. Summary of design parameters using in the study.

Parameter	Value
System power and flux constraint	50 MW _{th} at the design point with maximum flux of 130 W/m ²
Heliostats	Dimensions: 6.1 m length, 6.1 m width, Area: 37.21 m ² , Slope error: 1.5 mrad, Reflectivity: 0.95
Tower height and tilt angle	100 m from the heliostat pivot point to the center of the aperture. Tilt angle: 26° from the vertical
Receiver dimensions	17 m OD, 25 m height
Aperture	6 m width, 23 m height
Tube dimensions	0.0213 m OD, 0.01576 m ID
Tube emissivity & absorptivity	0.95
Insulation emissivity & absorptivity	0.60

in this case — from 400°C to 605°C and also provide the endothermic heat for the gasification reactions. The model implements a one-dimensional non-isothermal plug-flow reactor (PFR). Axial mixing of the reacting species, due to concentration gradients is not considered and mass transfer is by advection only. The change in composition of the supercritical phase with temperature and extent of reaction is accounted for at each point inside the reactor tube and the exit fluid is assumed to be a single phase supercritical mixture of syngas and H₂O. The thermochemical conversion of algae can be summarised as follows:



Algae (or any real biomass species) is a complex mixture of numerous biochemical constituents and appropriately modelling its properties is non-trivial. In this work, algae has been modelled using an approximate chemical formula, CH_xO_yN_z ($x = 1.71, y = 0.43, z = 0$), based on the ultimate analysis of algal species reported in literature [17]. It should be noted that we have not considered nitrogen-containing species in our analysis. The enthalpy of formation of algae is based on an empirical correlation for higher heating value (HHV) reported by Eboibi et al. [18]. Due to the lack of sufficient kinetics data in the temperature of interest, the kinetics have been assumed to be zeroth order and the product composition being predicted in accordance with the Gibbs free energy minimisation, with the non-negative moles constraint. We have used Peng–Robinson EoS with vdW mixing rules here, following the evaluation of Withag et al. [19], as it has previously been implemented and validated for modelling SCWG of biomass, glycerol and algae [20, 21]. The validation against experimental data and ASPEN predictions were reported previously [11]. The Gibbs function minimisation procedure can be summarised as:

$$G = \sum_{i=1}^n n_i \mu_i \quad (5)$$

$$\mu_i(T, P) = \mu_i^\circ(T) + \bar{R}T \log_n \left(\frac{\bar{f}_i}{f_i^\circ} \right) \quad (6)$$

$$\mu_i^\circ(T, P) = \bar{h}_{f,i}^\circ + \int_{298}^T \bar{c}_{p,i}(T) dT - T \bar{s}_{f,i}^\circ - T \int_{298}^T \frac{\bar{c}_{p,i}(T)}{T} dT \quad (7)$$

where μ_i and n_i are the chemical potential and mole number of each component; μ_i° , \bar{R} , and f_i° are the standard

molar chemical potential, universal gas constant and reference state fugacity of component i respectively; \bar{f}_i is the fugacity of component i and is calculated using van der Waals mixing rule. The chemical potential as a function of temperature and pressure is formulated as explained by Sandler [22].

The radiosity model is solved simultaneously with the equilibrium prediction and hydrodynamic model. Using the radiosity calculations, the surface temperatures are calculated, whereas the hydrodynamic model uses the incident flux boundary condition to solve for fluid and cavity-wall temperatures. The two models are run iteratively until a convergence on the surface temperatures predicted by the two models is achieved. The flow-rate of algae solution in each bank is optimised such that the outlet temperature of the fluid is 605°C. For calculation of stresses in the tube wall [23], the circumferentially varying temperature distribution, under steady-state, can be represented in terms of a plane harmonic Fourier series expansion, wherein the coefficients can be calculated by curve-fitting the circumferential temperature distributions at the inner and outer tube walls (Eqs. 8–9).

$$T_i = \bar{T}_i + \sum_{n=1}^{\infty} (B'_n \cos n\theta + D'_n \sin n\theta) \quad (8)$$

$$T_o = \bar{T}_o + \sum_{n=1}^{\infty} (B''_n \cos n\theta + D''_n \sin n\theta) \quad (9)$$

The contributions of pressure stresses and thermal stresses (both axisymmetric and non-axisymmetric components) can be calculated as described in Eqs. 10–14. Pressure stresses:

$$\sigma_r = \frac{p_i d_i^2}{d_o^2 - d_i^2} \left(1 - \frac{d_o^2}{r^2}\right); \quad \sigma_\theta = \frac{p_i d_i^2}{d_o^2 - d_i^2} \left(1 + \frac{d_o^2}{r^2}\right); \quad \sigma_z = \frac{p_i d_i^2}{d_o^2 - d_i^2} \quad (10)$$

Axisymmetric thermal stress component:

$$\sigma_r = \frac{\lambda E (\bar{T}_i - \bar{T}_o)}{2(1 - \nu) \log_n \frac{d_o}{d_i}} \left[-\log_n \frac{d_o}{r} - \frac{d_i^2}{d_o^2 - d_i^2} \left(1 - \frac{d_o^2}{r^2}\right) \frac{d_o}{d_i} \right] \quad (11)$$

$$\sigma_\theta = \frac{\lambda E (\bar{T}_i - \bar{T}_o)}{2(1 - \nu) \log_n \frac{d_o}{d_i}} \left[1 - \log_n \frac{d_o}{r} - \frac{d_i^2}{d_o^2 - d_i^2} \left(1 + \frac{d_o^2}{r^2}\right) \frac{d_o}{d_i} \right] \quad (12)$$

Non-axisymmetric thermal stress component:

$$\sigma_r = \frac{\lambda E}{2(1 - \nu)} \frac{r d_o d_i}{d_o^2 - d_i^2} \left[\left(\frac{B'_1 d_o - B''_1 d_i}{d_o^2 + d_i^2} \right) \cos \theta + \left(\frac{D'_1 d_o - D''_1 d_i}{d_o^2 + d_i^2} \right) \sin \theta \right] \left[\left(1 - \frac{d_i^2}{r^2}\right) \left(\frac{d_o^2}{r^2} - 1\right) \right] \quad (13)$$

$$\sigma_\theta = \frac{\lambda E}{2(1 - \nu)} \frac{r d_o d_i}{d_o^2 - d_i^2} \left[\left(\frac{B'_1 d_o - B''_1 d_i}{d_o^2 + d_i^2} \right) \cos \theta + \left(\frac{D'_1 d_o - D''_1 d_i}{d_o^2 + d_i^2} \right) \sin \theta \right] \left[\frac{d_i^2 d_o^2}{r^4} + \frac{d_i^2 + d_o^2}{r^2} - 3 \right] \quad (14)$$

Axial stresses can be calculated as:

$$\sigma_z = \nu(\sigma_r + \sigma_\theta) + \lambda E (\bar{T} - T) \quad (15)$$

In Eqs. 8–14, \bar{T} denotes the average circumferential temperatures, d_i and d_o are the inside and outside diameters of the reactor tubes, E is the Young's modulus, λ is the coefficient of linear expansion, and ν is the Poisson's ratio. The total stresses on the axially unconstrained reactor tubes are obtained using the superimposition of pressure and thermal stresses in the principle directions. Equivalent or von Mises stress is calculated from the orthogonal cylindrical (r , θ , z) stresses as:

$$\sigma_{eq} = \sqrt{\frac{1}{2} [(\sigma_r - \sigma_\theta)^2 + (\sigma_\theta - \sigma_z)^2 + (\sigma_z - \sigma_r)^2]} \quad (16)$$

The energy balance and the receiver efficiency is computed as follows:

$$\dot{Q}_{tot,aper_plane} = \dot{Q}_{aper} + \dot{Q}_{spillage} \quad (17)$$

$$\dot{Q}_{aper} = \dot{Q}_{wall_cond} + \dot{Q}_{refl} + \dot{Q}_{rad_loss} + \dot{Q}_{conv_loss} = \dot{Q}_{abs} + \dot{Q}_{refl} \quad (18)$$

$$\eta_{l,receiver} = \dot{Q}_{wall_cond} / \dot{Q}_{aper} \quad (19)$$

RESULTS AND DISCUSSION

The incident flux on the aperture plane is imposed by the heliostat field layout and the aiming strategy. Considering the chosen optical field parameters, there is an optimal geometry of the receiver which can minimise the exergy destruction in the receiver/reactor. This geometry is dependent on the flux distribution and also influenced by (a) the economical constraints such as manufacturing costs of complex receiver shapes, and (b) the thermo-mechanical limits of the reactor materials. As outlined in [11], the cavity shapes for on-sun SCWG of algae are limited by the peak flux on the tube walls (here taken as 130 W/m^2). Taking into account these flux limitations, an appropriate aiming strategy was used and the resultant incident flux map (after accounting for cavity reflections) is presented in Fig. 3(a).

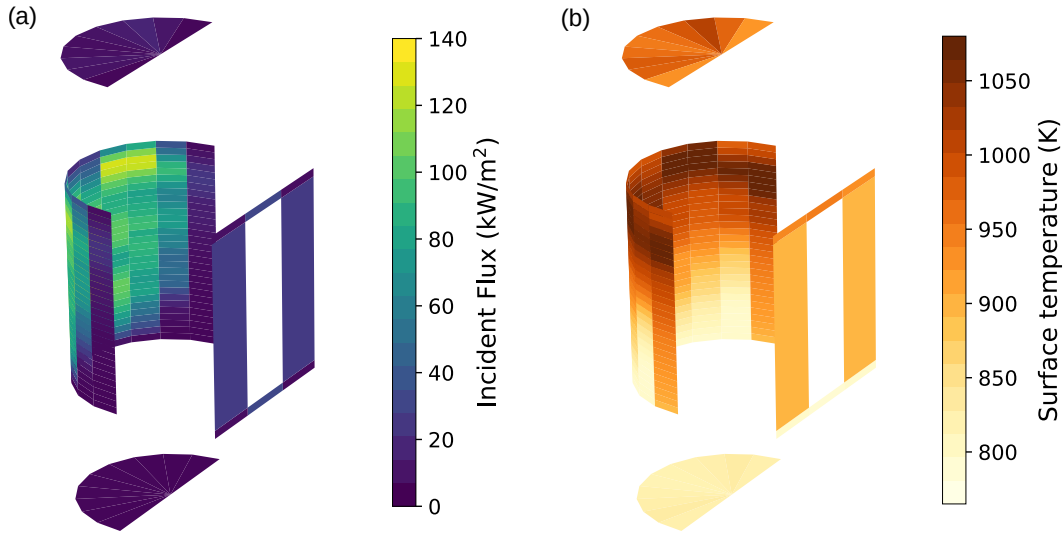


FIGURE 3. (a) Incident flux map accounting for reflections as well, and (b) Surface temperatures inside the cavity reactor under steady state.

The discretisation of cavity internal surfaces can be seen in Fig 3(a). Figure 3(b) shows the wall temperatures inside the cavity reactor. The peak temperature, under steady-state conditions, at the design point is $\sim 800^\circ\text{C}$ (1073 K). The feedstock flowrate in each bank is assumed different and optimised to achieve a fluid outlet temperature of $605 \pm 5^\circ\text{C}$ ($878 \pm 5 \text{ K}$).

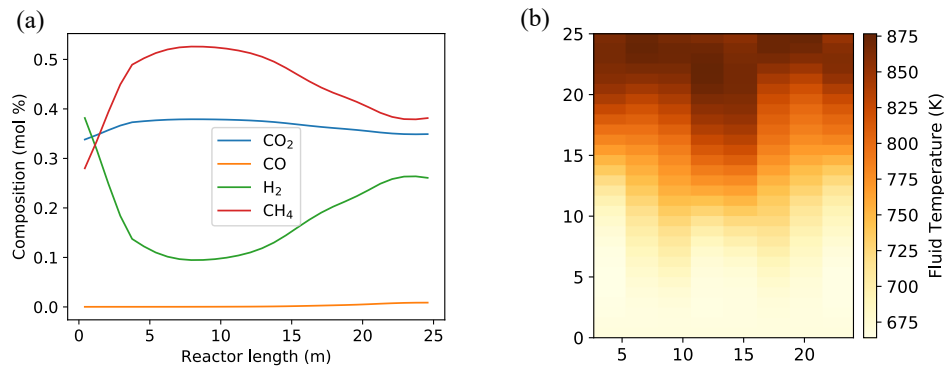


FIGURE 4. (a) Product composition along one representative fluid path, (b) Fluid temperature inside the tubes; one representative tube shown in each tube bank.

As mentioned previously, due to lack of temperature-dependent kinetics information for algae gasification, a zeroth order decomposition is assumed. Algae consumption is linear in the axial direction and the local equilibrium is evalu-

ated in each reactor element to predict the product gas composition. Figure 4(a) shows the evolution of product gases along the length of the reactor, whereas, Fig. 4(b) shows the fluid temperature along the reactor in each tube bank. For an isothermal gasification, low temperature and high feedstock concentration result in low H_2 and high CO_2 , CH_4 , and vice-versa. At the start of the reaction zone, the temperature is low, however, as a constant decomposition rate is assumed, this corresponds to a dilute feedstock scenario. Hence, the initial rate of H_2 -production in the reactor is observed. As the gas composition in the reactor changes, a decrease in H_2 content is observed, along with a corresponding increase in methane concentration. An increase in fluid temperature towards the end of the reaction zone, leads to higher H_2 and lower methane in the outlet product.

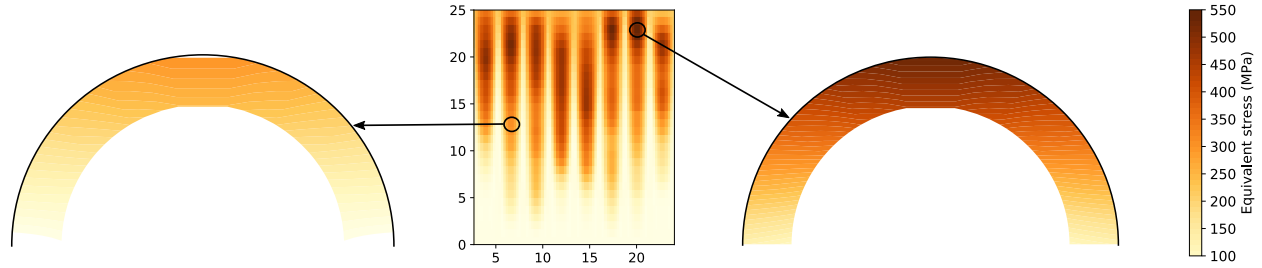


FIGURE 5. (a) Distribution of equivalent stresses on one tube section, (b) Maximum equivalent stress distribution in receiver tubes. One tube per bank is shown for better representation.

The total power incident on the aperture plane is 52.7 MW, of which spillage accounts for 16.7%. The receiver efficiency is ~66.7%, with the losses due to radiation, external convection and reflections accounting for 13.3%, 16.8% and balance respectively. The losses are quite high due to the large aperture-area and chosen aiming strategy, which were focused on achieving a uniform flux distribution. The equivalent stresses (pressure and thermal stresses) on the reactor tube walls, based on von Mises criterion, are shown in Fig. 5. For ease of representation, one tube per tube bank and only the front half is shown. The insets in Fig. 5 show a 2-d map of stresses on the front half of tubes, in two different locations inside the cavity. As expected the “crown” shows the highest equivalent stress for each tube section, with the peak value being ~530 MPa. It should be noted that the test case presented here corresponds to the summer solstice noon in Geraldton, WA. For higher solar irradiations, the peak stress would increase as well. This peak stress value is beyond the capabilities of the current generation of high temperature Fe- and Ni-based alloys. The results presented are not based on an optimised cavity shape and offers scope for addressing the allowable flux limits. Although the on-sun reactor modelled here is infeasible with current metallic alloys, the work highlights the fact that — with the inherent constraints on residence time (for complete gasification), incident flux and fluid outlet temperature — the design of an on-sun SCWG reactor would be extremely non-trivial.

CONCLUSION

An on-sun SCWG reactor presents an interesting challenge; the high pressure stresses due to the process conditions warrant thick tubes, which in-turn increases the thermal stresses, and coupled with the low heat transfer capabilities of the supercritical fluid, leads to a low peak flux requirement. In this work, we have attempted to present a complete analysis of the feasibility of a hemi-cylindrical cavity reactor for carrying out SCWG of algae. Even with a careful assessment of the controlling factors, the peak equivalent stress was of the order of 530 MPa, which is beyond the capabilities of current metallic materials. This paper presents Future work in this area is expected to be focused on novel design strategies, such as, (a) optimisation of tube arrangement [24] and multiple passes, (b) optimising cavity shape [16, 25], and (b) a cavity with tubes irradiated from both sides, so as to minimise the thermal stresses. Another approach would be to carry out the SCWG reaction off-sun. Each of these approaches present a significant challenge in terms of design/operation, and would be interesting to investigate from an optimisation perspective.

ACKNOWLEDGMENTS

This research was performed as part of the Australian Solar Thermal Research Initiative (ASTRI), a project supported by the Australian Government, through the Australian Renewable Energy Agency (ARENA).

REFERENCES

- [1] Carbon Dioxide Information Analysis Center, Environmental Sciences Division, Oak Ridge National Laboratory, Tennessee, United States. .
- [2] O. Yakaboylu, J. Harinck, K. Smit, and W. de Jong, *Energies* **8**, 859–894 (2015).
- [3] E. Gallagher, “The Gallagher Review of the indirect effects of biofuels production,” Tech. Rep. (Renewable Fuels Agency, 2008).
- [4] M. Brandenberger, J. Matzenberger, F. Vogel, and C. Ludwig, *Biomass and Bioenergy* **51**, 26–34 (2013).
- [5] A. Ganany, A. Kribus, A. Ullmann, and M. Epstein, “Improved Efficiency in Super-Critical Water Gasification (SCWG) Cogeneration,” in *SolarPACES 2011* (2011), pp. 2–3.
- [6] A. Rahbari, M. B. Venkataraman, and J. Pye, *Applied Energy* **228**, 1669–1682 (2018).
- [7] J. Chen, Y. Lu, L. Guo, X. Zhang, and P. Xiao, *Int. J. Hydrogen Energy* **35**, 7134–7141 (2010).
- [8] B. Liao, L. Guo, Y. Lu, and X. Zhang, *Int. J. Hydrogen Energy* **38**, 13038–13044 (2013).
- [9] H. Jin, Y. Lu, B. Liao, L. Guo, and X. Zhang, *Int. J. Hydrogen Energy* **35**, 7151–7160 (2010).
- [10] L. Guo, H. Jin, Z. Ge, Y. Lu, and C. Cao, *Sci. China Technol. Sci.* **58**, 1989–2002 (2015).
- [11] M. B. Venkataraman, A. Rahbari, and J. Pye, “Thermodynamic Modelling and Solar Reactor Design for Syngas Production through SCWG of Algae,” in *AIP Conf. Proc., Vol. 1850, Issue 1* (2017) p. 100017.
- [12] NREL, Solar PILOT, <https://www.nrel.gov/csp/solarpilot.html>, Accessed 21 Aug, 2018, .
- [13] Y. Meller, “Tracer package: an open source, object oriented, ray-tracing library in python language - original package -,” (2013), <https://github.com/yosefm/tracer>.
- [14] C.-A. Asselineau, “Tracer package: an open source, object oriented, ray-tracing library in Python language - Current development version -,” (2018), <https://github.com/casselineau/Tracer>.
- [15] M. F. Modest, *Radiative Heat Transfer*, edited by Elsevier (Academic Press, 2003).
- [16] C.-A. Asselineau, J. Zapata, and J. Pye, *Energy Procedia, SolarPACES 2014* **69**, 279 – 288 (2015).
- [17] Q. Guan, C. Wei, and P. E. Savage, *Physical Chemistry Chemical Physics* **14**, p. 3140 (2012).
- [18] B. E. Eboibi, D. M. Lewis, P. J. Ashman, and S. Chinnasamy, *Bioresource Technology* **170**, 20–29 (2014).
- [19] J. A. M. Withag, J. R. Smeets, E. a. Bramer, and G. Brem, *J. Supercrit. Fluids* **61**, 157–166 (2012).
- [20] O. Yakaboylu, J. Harinck, K. G. Smit, and W. D. Jong, *Energy & Fuels* **28**, 2506–2522 (2014).
- [21] D. Castello and L. Fiori, *Bioresource Technology* **102**, 7574–7582 (2011).
- [22] S. I. Sandler, *Models for Thermodynamic and Phase Equilibria Calculations* (CRC Press, New York, 1993) p. 704.
- [23] W. R. Logie, J. D. Pye, and J. Coventry, *Solar Energy* **160**, 368–379 (2018).
- [24] R. Dunn, K. Lovegrove, G. Burgess, and J. Pye, *Journal of Solar Energy Engineering* **134**, p. 041007 (2012).
- [25] C.-A. Asselineau, “Geometrical optimisation of receivers for concentrated solar thermal systems.” PhD. Thesis, Research School of Engineering, Australian National University 2017.